Tropical Instability Waves in the Atlantic Ocean: investigating the relative role of sea surface salinity and temperature from 2010 to 2018

Léa Olivier, Gilles Reverdin, Audrey Hasson, Jacqueline Boutin

Tropical Instability Waves in the Atlantic Ocean: investigating the relative role of sea surface salinity and temperature from 2010 to 2018

L. Olivier[1], G. Reverdin[1], A. Hasson[1,2] and J. Boutin[1]

[1]Sorbonne Université, CNRS, IRD, MNHN, UMR 7159, Laboratoire d'Océanographie et du Climat : Expérimentations et Approches Numériques, LOCEAN-IPSL F-75005, Paris, France

[2]Université de Toulouse, CNES, CNRS, IRD, UPS, Laboratoire d'Etudes en Géophysique et Océanographie Spatiales (LEGOS), Toulouse, France

Corresponding author: Léa Olivier (lea.olivier@locean-ipsl.upmc.fr)

Key Points:

- Satellite and in situ data highlight large seasonal and interannual variability in the respective roles of salinity and temperature on TIWs
- TIWs maximum surface salinity signal leads the temperature one by one month
- In the top 60-m of the ocean, salinity and temperature each contribute to about 50% of the TIWs perturbation potential energy

Abstract

We identify and analyse tropical instability waves (TIWs) in the equatorial Atlantic Ocean during 2010-2018 using satellite derived observations of sea surface salinity (SSS), sea surface temperature (SST), sea level anomaly and Argo profiles. In particular, the weekly 50-km resolution SSS time series from the climate change initiative project provides an unprecedented opportunity to observe the salinity structure at a scale closer to the SST scale. We examine the relative contributions of SSS and SST to the horizontal surface density gradient on seasonal and interannual time scales and how they contribute to the TIW properties and energetics. For the central Atlantic TIWs, the maximum of the SST contribution to the density anomaly lags the SSS one by approximately one month. Argo vertical profiles indicate that temperature and salinity both significantly contribute to TIW-related density anomalies. In May-June, salinity contributes to 50% of the perturbation potential energy (PPE) in the top 60-m, and between 30 and 45 % from July to September. While variations in SST appear to be related to dynamic processes, the interannual variability of SSS is also influenced by precipitations. However, the two leading modes of variability in the region (Atlantic Meridional and Zonal modes) do not well explain at 1°N these interannual variations.

Plain Language Summary

Density is a key variable, influenced by both salinity and temperature and essential to understand the equatorial Atlantic dynamics. Each spring and summer, the horizontal density gradient generated by the equatorial upwelling is subject to undulations associated with tropical instability waves (TIWs). These waves are important features that influence both the ocean dynamics and air-sea interactions.

The scarcity of historical salinity observations has been a limiting factor in the study of the relative role of salinity and temperature (and therefore density) in the TIWs dynamics. To do so, we use here an unprecedented 9-year satellite-based sea surface salinity dataset together with sea surface temperature and in situ Argo floats data.

We show that the Atlantic TIWs seasonal and interannual variations are different in salinity and temperature. The TIWs surface salinity seasonal cycle leads the temperature one by one month. Concerning the wave energetics, salinity is responsible for almost half of the potential energy generated by the density gradient. Contributions of temperature and salinity are similar in May and June, while temperature dominates in July to September. Further characterization of the seasonal cycle, interannual variations and energetics of TIWs will be necessary to better understand their role in climate.

1 Introduction

Ocean salinity is one of the key variables governing the density-driven global circulation, which in turn redistributes heat around the globe (Durack et al., 2012). In the tropical Atlantic Ocean, horizontal salinity gradients contribute much to density gradients and therefore to the large scale ocean circulation's baroclinicity (Murtugudde & Busalacchi, 1998; Foltz et al., 2004; Johnson et al., 2012; Lee et al., 2014). Horizontal surface salinity gradients are present in the tropical Atlantic for a large range of scales (Reverdin et al., 2007; Grodsky et al., 2014; Kolodziejczyk et al., 2015). At basin scale, the strongest horizontal salinity gradients are observed between the tropics and the subtropics. This is due to a combination of four main processes: (1) the high evaporation rates of the northern subtropics and south of the equator, (2) the Amazon's outflow which water spreads north of the equator, (3) the tropical rainfall excess north of the equator (Da-Allada et al., 2013; Yu, 2015), as well as (4) advection by a complex current system. The

near-surface ocean circulation of the region is indeed dominated by a series of seasonally varying currents and countercurrents bounded by the equatorial edges of the northern and southern subtropical gyres (Lumpkin & Garzoli, 2005; Behera et al., 2013). The tropical Atlantic Ocean is furthermore characterized by a strong mesoscale activity (Chelton et al., 2011) playing a major role in the transport of physical and chemical properties, such as heat, salt and nutrients and presenting strong horizontal gradients.

Close to the equator, horizontal gradients are especially strong because of the presence of the Atlantic cold tongue in spring and summer (Camara et al., 2015; Da-Allada et al., 2017) and the seasonal migration of the Intertropical Convergence Zone (ITCZ). Therefore, salinity does not only vary in space but also with time. In spring and summer this region is subject to strong current shears: between the North Equatorial Counter Current (NECC) and the northern branch of the South Equatorial Current (SEC) at the surface, and between the SEC and the Equatorial Undercurrent (EUC) at subsurface. At the end of the 1970's, Düing et al. (1975) and Legeckis (1977) observed that the meridional position of the temperature front associated with the Atlantic (and Pacific) cold tongue was subject to intraseasonal horizontal fluctuations due to tropical instability waves (TIWs). This discovery fuelled numerous studies based on satellite and in-situ observations, as well as on models. Located within a few degrees of the equator, these waves propagate westward with a time-period of 20-30 days and a wavelength on the order of a thousand kilometres (Legeckis & Reverdin, 1987; Steger & Carton, 1991; Qiao & Weisberg, 1995). They have a marked seasonal variability, peaking in July (Jochum et al., 2004), as well as an interannual variability influenced to a certain extent by the El Niño phenomenon in the Pacific (An, 2008; Im et al., 2012) and Atlantic Niño in the Atlantic (Perez et al., 2012).

89 TIWs have a strong influence on their environment. Indeed, through air-sea coupling they
90 interact with the winds, clouds and precipitations at local scales (Chelton et al., 2001; Caltabiano
91 et al., 2005; Seo et al., 2007; Wen et al., 2012). Their associated transports contribute to the
92 warming of the mixed layer in the equatorial band (Jochum et al., 2007), as the equatorward heat
93 flux generated by the TIWs in the upper 50-m approximately reaches 100 $W.m^{-2}$ (Weisberg &
94 Weingartner, 1988) which is comparable to the atmospheric heat flux in the tropics. They also
95 play an important role in the heat exchanges between the surface and the deep ocean (Jochum &
96 Murtugudde, 2006). TIWs are associated with an undulation of the chlorophyll front (Strutton et
97 al., 2001; Jochum et al., 2004) and through their effect on the nutrient distribution (Murray et al.,
98 1994), they impact the development of marine ecosystems (Menkes et al., 2002; Martinez et al.,
99 2018). TIWs hence are important dynamical features that influence the air-sea interactions and
100 biogeochemistry of the tropical Atlantic Ocean. CMIP (Coupled Model Intercomparison Project)
101 models suggest that Atlantic TIWs will be energized under global warming scenarios (Seo &
102 Xie, 2011). Further investigating TIWs from observations would therefore provide useful
103 information to improve their representation in models (Ham & Kang, 2011).

104 Historically, TIWs were first detected from Sea Surface Temperature (SST) and current
105 observations (Düing et al., 1975; Legeckis, 1977). They have then been observed in sea surface
106 height (Musman, 1992; Katz, 1997), and they have also recently been observed in Sea Surface
107 Salinity (SSS) from novel satellite missions, both in the Pacific (Lee et al., 2012; Yin et al.,
108 2014) and in the Atlantic (Lee et al., 2014).

109

110 TIWs extract their energy through interactions with the mean background state. Some studies
111 proposed that the undulations of the SST front associated with TIWs originate from barotropic
112 instabilities fuelled by the shear of the tropical currents system: between the NECC and the

northern branch of the SEC (Philander, 1976, 1978; Weisberg & Weingartner, 1988; Kelly et al., 1995; de Decco et al., 2018) and between the SEC and the EUC (Jochum et al., 2004; Von Schuckmann et al., 2008). Several studies show nevertheless the importance of baroclinic instabilities in the generation of TIWs (e.g. Cox, 1980; McCreary Jr & Yu, 1992; Grodsky et al., 2005). The baroclinic conversion indeed makes the density gradient contribute to the energetics of the TIWs. It represents the energy conversion between the background available potential energy (APE) and the perturbation potential energy (PPE). The accurate representation of the horizontal density gradient has been a great limitation in studying the importance of baroclinic instabilities in the past. Most observation-based studies (e.g. Weisberg & Weingartner, 1988) did not consider the effects of salinity because of the scarcity of observations. Grodsky et al. (2005) based on data from a single mooring showed that salinity contributed to the energetics of the TIWs in the mixed layer. Lee et al. (2014) supported this observation and drew a first estimate of the salinity gradient contribution to the wave's PPE at basin scale based on unprecedented satellite observations. However, the computation of the energy associated with the waves based solely on surface observations implies strong assumptions on the contribution of salinity and temperature to the density gradient at depth.

The main objective of this study is therefore to investigate the TIWs properties and energetics in the Atlantic Ocean. This study takes advantage of a combination of SSS, SST and sea level anomaly products from remote sensing, as they provide a full dynamical spatial and temporal sampling of the wave surface variability. In particular, the most recent satellite-borne SSS dataset combining the observations of three missions enables us to perform this study over a 9-year period (2010-2018) at a horizontal resolution close to 50 km and at a weekly time scale. The satellite and in-situ data from Argo float profiles are furthermore associated in order to have the

most accurate representation of the TIWs' horizontal and vertical structure as well as seasonal variability.

This paper is organized as follows. In section 2, the satellite and in situ data products are presented as well as the methodology. Results are reported in the four subsections of section 3. The first subsection presents the analysis of the propagating characteristics and spatial structure of TIWs. The variability on seasonal timescales of TIW signature in SSS and SST and their respective contribution to the density gradient is presented in subsection 3.2, while the interannual variability of TIWs is described in subsection 3.3. The relative contribution of salinity and temperature on the TIW energetics is characterized in subsection 3.4, by estimating the PPE integrated over the upper water column impacted by TIWs. Section 4 discusses the results and section 5 concludes and underlines the limits of this study.

2 Materials and Methods

2.1 Data

We use satellite-derived SSS, SST, chlorophyll (Figure 1), sea level anomaly and precipitation datasets, as well as in situ data from Argo floats. These datasets are presented below.

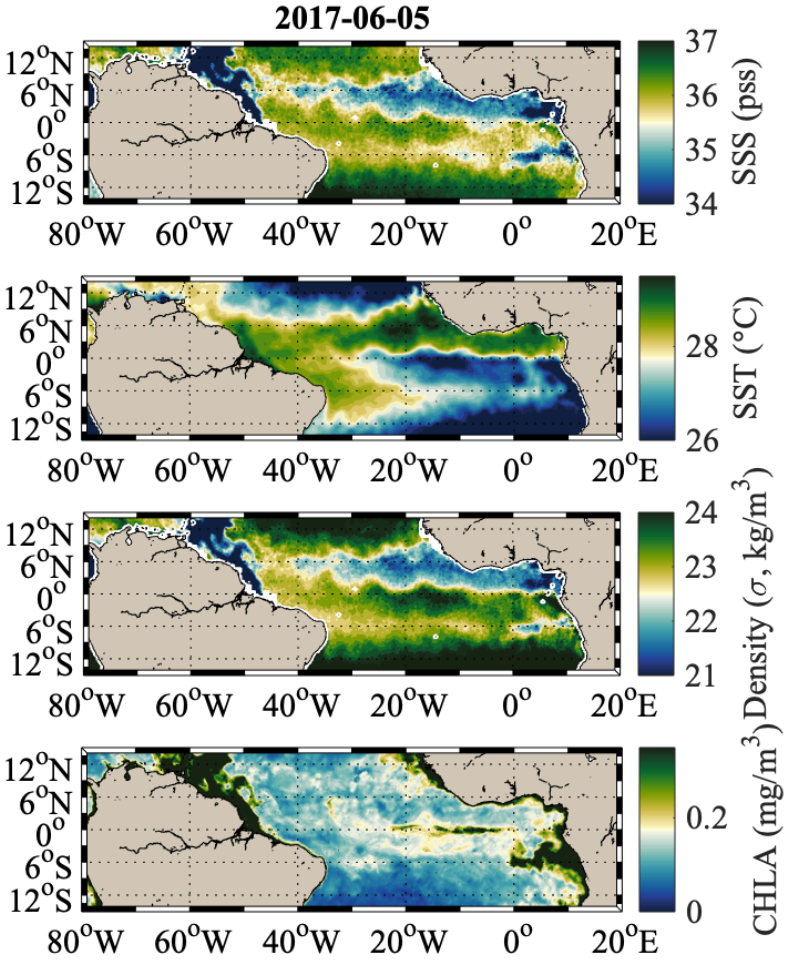

Figure 1: *5th June 2017 snapshot of a) sea surface salinity, b) sea surface temperature, c) sea surface density ($\sigma = density - 1000\ kg/m^3$), d) surface chlorophyll.*

A core product for this study is the ESA CCI (European Space Agency Climate Change Initiative) version 1.8 Sea Surface Salinity (Sea_Surface_Salinity_cci) available from 2010 to 2018 (Boutin et al., 2019). It provides, at near-global scale, integrated homogenised multi-mission time series of SSS data. It is a long-term multi-mission salinity Climate Data Record based on a temporal optimal interpolation of three L-Band radiometric missions: the Soil Moisture and Ocean Salinity (SMOS, Jan. 2010-present), Aquarius/SAC-D (Aug. 2011; June 2015) and the Soil Moisture Active Passive (SMAP, Apr. 2015-present). Systematic

discrepancies between different satellite acquisitions in various geometries are adjusted in a similar way as the adjustments applied to SMOS datasets available at Centre Aval de Traitement des Données SMOS (Boutin et al., 2018). The European SMOS mission consists of a sun-synchronous polar-orbiting satellite (Font et al., 2009; Kerr et al., 2010; Reul et al., 2020). Its orbit covers the entire globe within 3 days and the retrieved SSS has a spatial resolution of ~45 km. The Aquarius/SAC-D mission was developed collaboratively between NASA (National Aeronautics and Space Agency) and Argentina's space agency, Comisión Nacional de Actividades Espaciales (CONAE). Aquarius has a 7-day repeat cycle and provides SSS data with a spatial resolution on the order of 150 km (Lagerloef et al., 2008). Developed by NASA, SMAP mission covers the entire globe in 3 days, and has a spatial resolution of ~40 km (Entekhabi et al., 2010; Piepmeier et al., 2017). The merged SSS CCI product dataset used in the present study has therefore an effective resolution of nearly 50 km. It is smoothed with a 7-day Gaussian filter and is sampled daily on a 25-km EASE (Equal Area Scalable Earth) grid. The TIWs interannual variability in the CCI dataset is coherent with the one observed by the individual satellites (supplementary Figure S1). The CCI v1.8 used in this study is very similar in our area of interest to the recently available CCI v2.3. Therefore, no significant changes of the results on TIWs and salinity structures are expected.

The Operational Sea Surface Temperature and Sea Ice Analysis (OSTIA) SST product, distributed by the Copernicus Marine and Environment Monitoring Service (CMEMS) combines satellite data provided by the Group for High Resolution Sea Surface Temperature (GHRSST) project, together with in-situ observations (Donlon et al., 2012). The analysis is performed using a variant of optimal interpolation described by Martin et al. (2007). Daily maps of SST are produced at a resolution of 1/20° (approx. 5 km). OSTIA SST uses most SST data available for a

day, from both infrared and microwave inferred SST. This product is available from 1981 to present.

Sea level anomaly maps are produced by Ssalto/Duacs and distributed by CMEMS. Sea level anomaly is mapped using an optimal interpolation method. It is produced daily on a 0.25°x 0.25° grid. The product chosen (SEALEVEL_GLO_PHY_L4_REP_OBSERVATIONS_008_047) combines data from all satellites available for the period 1993 to present.

We also use rainfall data from the Global Precipitation Climatology Project (GPCP) in its version 2.3. This product merges data from rain gauge stations, satellites, and sounding observations to estimate monthly rainfall. Precipitations are then available on a 2.5° global grid from 1979 to present, and a monthly climatology over the years 2010-2018 is made. The GPCP data is provided by the NOAA/OAR/ESRL PSD (Adler et al., 2003).

Surface chlorophyll data are the GlobColour dataset derived from ocean color at a 1/24° resolution. It is a merged product from multiple satellite missions observations (SeaWiFS, MERIS, MODIS, VIIRS NPP, OLCI-A, VIIRS JPSS-1 and OLCI-B; Maritorena et al., (2010)). GlobColour data is developed, validated, and distributed by ACRI-st.

In addition to the satellite-based data, we use Argo float temperature and salinity (flagged as good) profiles located in the band 0°N-3°N, 10°W-30°W from January 2010 to December 2018 (supplementary Figure S2). All Argo float profiles for the period and area of interest (648 in total) are interpolated with a 1-m resolution. The top 5-m measurements are discarded due to the lack of numerous good quality data close to the surface and the value at 6 m is extrapolated to the surface.

2.2 Methods

Various studies have shown that the most energetic TIWs have frequency and wavelength in the equatorial band in the 20-50 day period range and close to 10° zonal wavelength (Legeckis & Reverdin, 1987; Steger & Carton, 1991; Qiao & Weisberg, 1995; Jochum et al., 2004). In order to detect changes due to the TIWs variability (and following the approach proposed by Lee et al. (2014)), SSS, SST and sea level anomaly data are filtered with a 20-50 day 0-phase second order Butterworth band-pass filter. Further very long wavelength zonal variability structures are removed with a 20° high-pass second order 0-phase Butterworth filter. These long wavelength structures are particularly intense in the first half of the year. Special treatment was applied to SSS in order to reduce the noise and enhance the signal of the SSS gradient in the central tropical Atlantic: SSS data are averaged over 5 pixels (5x0.25°) in longitude, on the basis of a comparison with ship-mounted thermosalinograph and satellite data presented in the supplementary information (Figure S3). For all variables the amplitude (envelope) of the wave packet is deduced from the filtered TIW anomalies. We assume that the filtered signal can be approximated by a harmonic wave

$$A(t)\,cos(\omega t + \phi)\,, \qquad (1)$$

where $A(t)$ is the amplitude, ω the local pulsation, and ϕ the local phase. $A(t)$ varies with a time period T longer than the one of the waves. From the cosine function properties, the temporal mean of squared cosine is $\frac{1}{2}$ over one period. Therefore, a low-passed Ã(t) is estimated as:

$$\tilde{A}(t) = \left(\frac{2}{T}\int_0^T dt\, A^2(t)\cos^2(\omega t + \phi\right)^{1/2}, \qquad (2)$$

the integration over the time period T is achieved through a 50-days, 0-phase second-order low-pass Butterworth filter.

In order to compute the PPE generated by the horizontal density gradient, Argo profiles from 2010-2018 and between 10°W-30°W and 0°N-3°N (black box in Figure 2) are sorted into two categories (positive and negative) based on the sign of the filtered density anomalies. These anomalies for the 5th of June 2017 are represented in Figure 2. Mean profiles of salinity, temperature and density associated with positive (t_+, s_+, ρ_+) and negative (t_-, s_-, ρ_-) density anomalies are computed for each month (supplementary Figure S4).

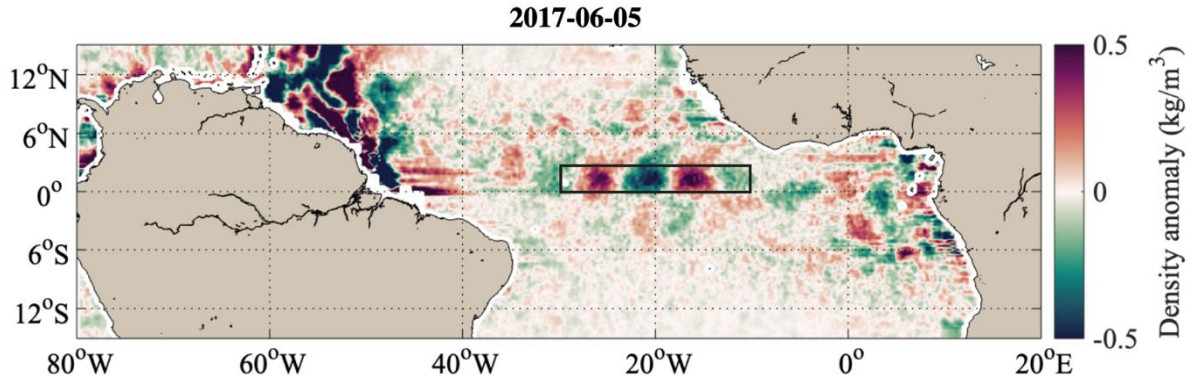

Figure 2: *Snapshot of the density anomaly on the 5th of June 2017. The black square corresponds to the region where Argo profiles are selected.*

Since Argo float profiles are not evenly distributed, the mean profiles located in positive and negative surface density anomaly for each month are not at the same latitude-longitude. The strong meridional and zonal gradients in spring and summer can bias the results. To avoid this, we divided the large 30°W-10°W longitude band into four smaller bands (30°W-25°W, 25°W-20°W, 20°W-15°W and 15°W-10°W) and neglected the zonal gradients in each band. The mean meridional gradient of temperature and salinity is then estimated from the Argo data set for each couple of months, at each depth and in each band. Mean profiles t_+, s_+, ρ_+ and t_-, s_-, ρ_- are computed for each month, in each band, corrected from the mean meridional gradient and then averaged over the four longitude bands.

In the thermocline near the depth of the core of the EUC (near 60 m), the scatter of temperature and salinity between the different profiles becomes large. This results in large uncertainties (supplementary Figure S5) in the composite monthly profile, so we will not interpret the results deeper than 60 m. The results do not change significantly for a small variation of this limit, but would be impacted if the change is on the order of tens of meter as PPE is sensitive to density anomalies at depth. To characterize the density layer directly influenced by salinity anomalies, the top 60 m is divided into two layers: surface to 35 m, and 35 m to 60 m. The 35-m limit is chosen based on the comparison between the positive and negative salinity profiles for the months of May, June, July, August and September. It corresponds on average to the depth where the signal is inferior to 90% of the surface one (the vertical salinity gradient is close to 0) and therefore above which surface anomalies are rather evenly distributed in the water column. A variation of a few meters of this limit does not change significantly the results presented in part 3.4.

The PPE of the water column is defined as the vertical integral of the potential energy associated to a small density perturbation (Lorenz, 1955; Kang & Fringer, 2010):

$$PPE = \int_{-60}^{0} \rho' g z dz \quad (3)$$

with ρ' the density perturbation computed as $\rho' = \rho_+ - \rho_-$, g the acceleration constant and z the depth in the water column. We are investigating an instability intensified in the upper water column, we therefore integrate from the surface to the EUC depth (60 m). Moreover, below 60 m uncertainties become larger than the difference between the positive and negative profiles (ρ', S' and T', Figure S5). We separate the contribution of salinity and temperature to the density perturbation as:

$$\rho' = \rho_0 \cdot \beta \cdot S' - \rho_0 \cdot \alpha \cdot T'$$

With $S' = S_+ - S_-$, $T' = T_+ - T_-$, $\rho_0 = 1025$ kg/m^3 the reference density, α the thermal expansion coefficient and β the haline contraction coefficient computed from the mean temperature and salinity profiles for each month. Therefore, the relative contributions of salinity and temperature to the integrated PPE are, for salinity and temperature respectively:

$$\int_{-60}^{0} \rho_0 \beta S' g z dz \quad (4)$$

and

$$-\int_{-60}^{0} \rho_0 \alpha T' g z dz \quad (5).$$

To calculate the available potential energy (APE) generated by the background meridional density gradient, and the contribution of temperature and salinity, we adopt a similar method to the PPE. Instead of calculating the energy associated with the deviation of the mean density profile by a TIW perturbation, we look at the energy associated with the deviation by the meridional gradient of the mean density profile. For each band in longitude we define $\rho'' = \rho_S - \rho_N$ where ρ_S represents the mean density profile in the 0°-1.5°N box and ρ_N the one in the 1.5°-3°N box. We then average over the four longitude bands. By replacing ρ' by ρ'' in equation (3) we obtain the APE computed on the top 60 m. The contribution of temperature and salinity to APE are calculated in a similar way by replacing S' and T' by $S'' = S_S - S_N$ and $T'' = T_S - T_N$ in equations (4) and (5).

3 Results

3.1 Observations and properties of tropical instability waves

Figure 1 represents a typical situation at the end of boreal spring on June 5th 2017 and illustrates the main large-scale and mesoscale horizontal gradients in the tropical Atlantic. The SSS structures reveal the influence of the Amazon's outflow on the western side of the basin. In early June, the just-set North Brazil Current retroflection (8°N-54°W) barely advects any fresh water eastward. The ITCZ, located near 4°N, begins to shift northward and contributes to the band of fresh water between 2°N and 6°N. Around the equator, salty water is brought to the surface by the upwelling system. Mesoscale features such as the cusp-like deformations of the SSS gradient are present around 1°N, with a difference of up to 1 pss between the two sides of the cusp. These features are a trademark of the TIWs and are also observed in both SST (Figure 1b), with a difference of over 2°C across the cusps, and surface density (Figure 1c) with a difference of over 2 kg/m^3 across the cusps.

The correspondence between SSS and SST features associated with TIWs and surface chlorophyll (Figure 1d) corroborates previous studies showing that TIWs play a large role in the biogeochemical processes in the equatorial Atlantic (e.g. Menkes et al., 2002).

Westward propagation along 1°N is found on all data sets, when filtered to retain the 20-50 days periods and 0°-20° wavelengths in order to highlight the TIWs (Figure 3). It has been previously shown that TIWs in the Atlantic are particularly intense at 1°N (Chelton et al., 2000; Lee et al., 2014) and it is also the case in the data used for this study. We nevertheless observe a shift of the SST and SSS front toward the equator in the East and away from the equator in the West

311 (supplementary Figures S6, S7 and S8). Between 2010 and 2018, we observe the presence of
312 TIWs at 1°N every year in SST, SSS and sea level anomaly.

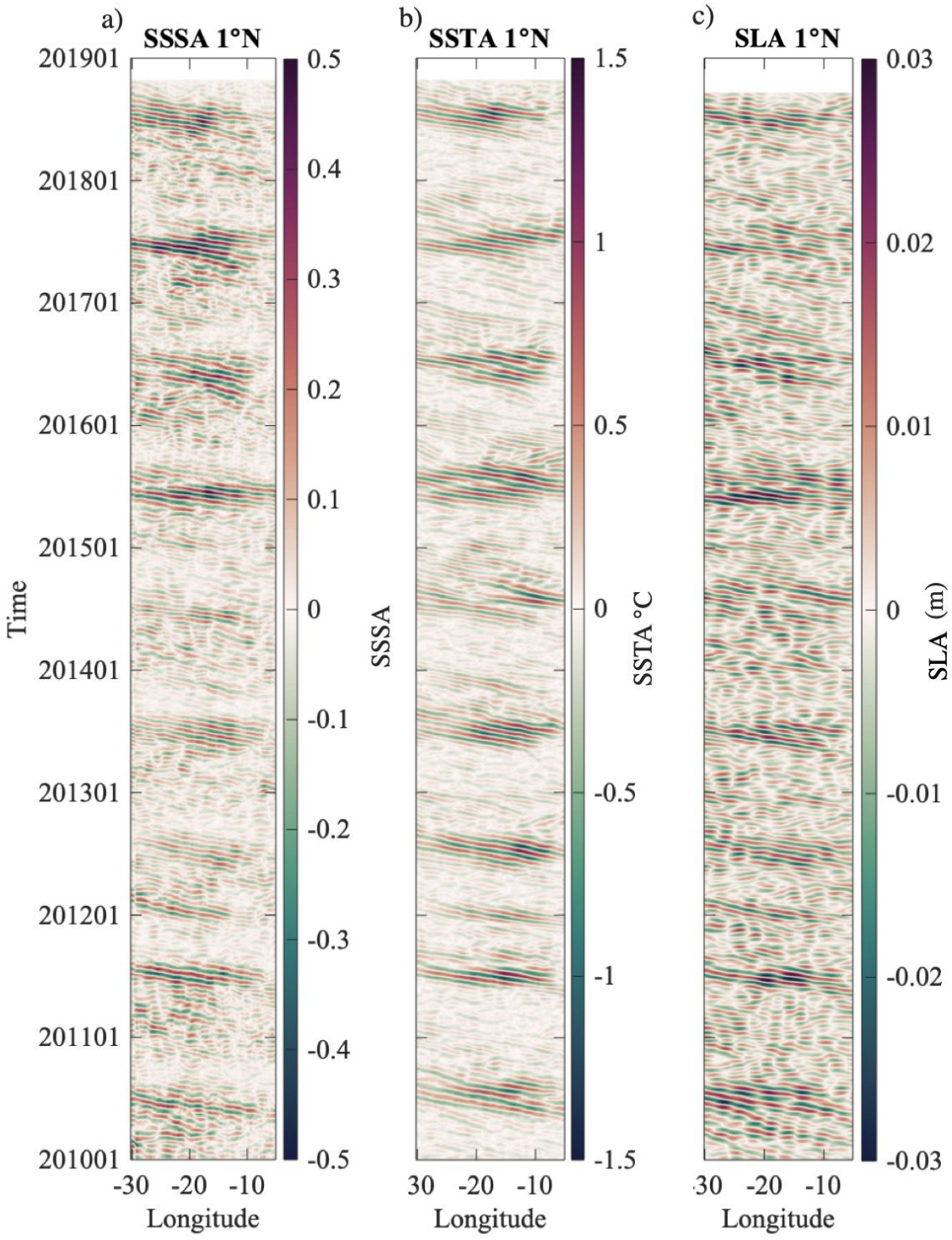

313

314 ***Figure 3:*** *2010-2018 Hovmöller diagrams at 1°N of a) sea surface salinity anomaly, b) sea surface temperature*
315 *anomaly, c) sea level anomaly.*

3.2 Seasonal variability of TIWs signature in SSS and SST and their contribution to the density gradient

The seasonal climatologies of the amplitude of the 9-year SSS, SST and SLA TIW-anomalies (SSSA, SSTA, SLA) are represented in Figure 4. The altimeter sea level is a deviation from the local time-mean (hence the notion of sea level anomaly), thereafter we will use SLA to refer to the TIW-anomalies of sea level. TIWs are present in all datasets during the same season (May-September) and are almost non-existent during boreal winter. On average, they reach half of their maximum amplitude on the 5th of May in SSS, 19th of May in SLA and 1st of June in SST. TIWs gradually get more intense (as visible in the amplitude of SLA, Figure 4c), and reach a peak in July. Their amplitude then decreases and is significantly dampened (half of the maximum amplitude) by the 1st of August in SSS (a duration of 88 days), 11th of August in SLA (a duration of 84 days) and 21st of August in SST (a duration of 81 days). The SSSA amplitude average is 0.3 pss, with a maximum 0.53 pss in June 2015. The SSTA amplitude average is 0.7°C and reaches 1.3°C in July 2012 (Figure 3). The 2011-2012 period stands out as a winter event of TIWs is observed (Figure 3, visible on all datasets).

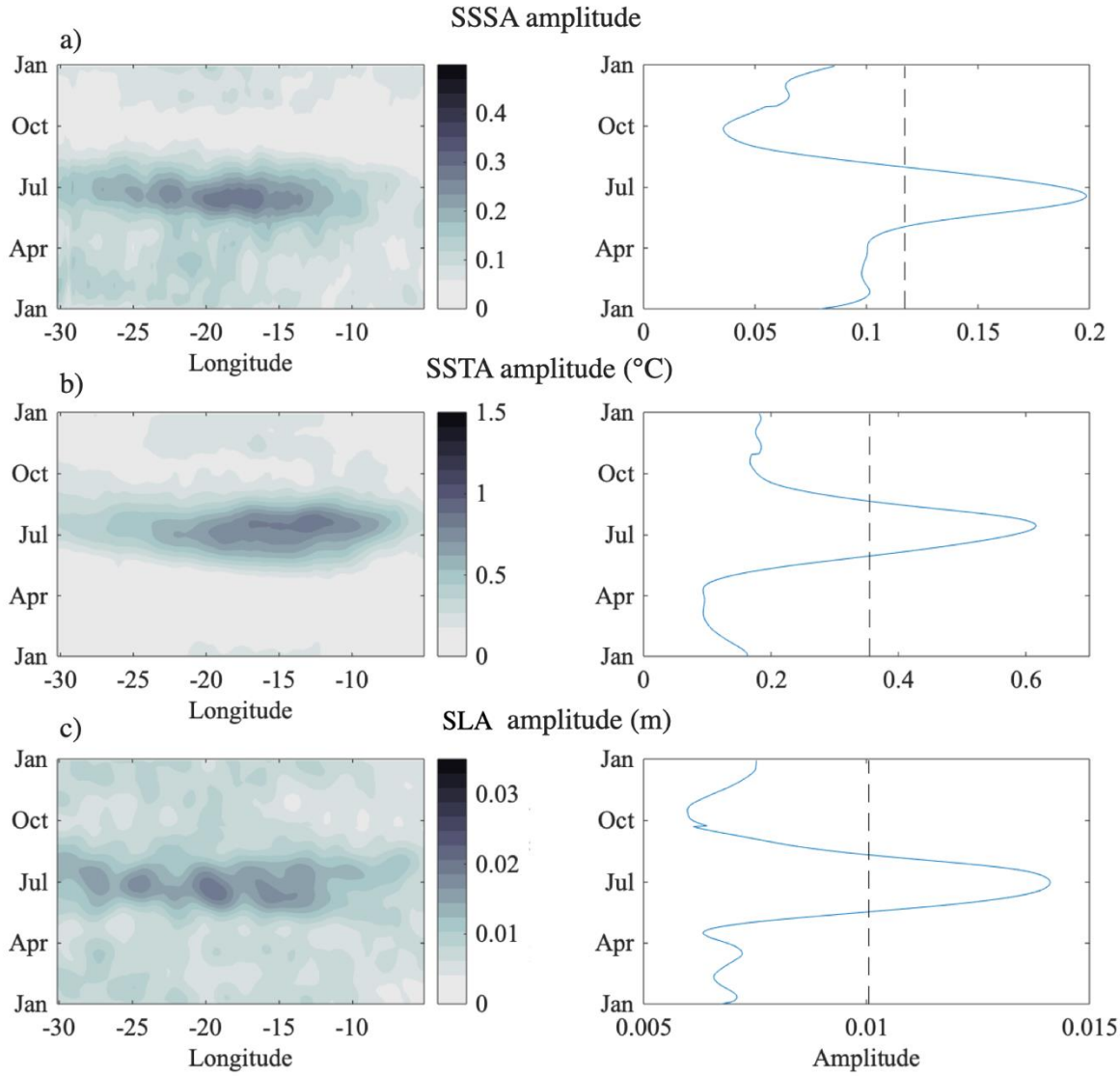

Figure 4: *Hovmöller diagram of the 2010-2018 a) SSSA amplitude climatology, b) SSTA amplitude climatology, c) SLA amplitude climatology at 1°N (left) and corresponding longitude averaged monthly climatology (right). The dashed line corresponds to half of the maximum amplitude.*

We investigate the seasonal variability of both SST and SSS and their relative contribution to surface density (respectively $\rho(SSTA)$ and $\rho(SSSA)$). By linearizing the equation of state for sea water (small variations of the density) at the surface with respect to a mean state, we have the following relation:

$$\rho = \rho_0[1 - \alpha(T - T_0) + \beta(S - S_0)] \quad (6)$$

Therefore $\rho(SSSA) = \rho_0 \cdot \beta \cdot SSSA$, (7)

and $\rho(SSTA) = -\rho_0 \cdot \alpha \cdot SSTA$ (8)

where α and β are fixed and computed with T_0 (26.1°C) and S_0 (35.8 pss) the mean values of SST and SSS for the season and region investigated. Changes in thermal and haline coefficients due to the seasonal and interannual SST changes are neglected as they are relatively small here.

At first order, $\rho(SSTA)$ is only slightly higher than $\rho(SSSA)$ (by 0.05 kg/m^3, Figure 5). In 2017, $\rho(SSSA)$ is even higher than $\rho(SSTA)$. The surface density gradient is significantly influenced by salinity in 2012-2013, as observed by Lee et al. (2014). This result is relevant for all years, and the contribution of SSS to the TIW density gradient was even smaller in 2012-2013 than the 9-year average. At the surface, the contribution of salinity to the horizontal density gradient is comparable to the one of temperature and thus not negligible.

On average the TIW signal appears 27 days earlier in SSS than in SST (Figure 4). The relatively weak SST gradient in spring allows the strong SSS gradient to significantly influence the density gradient. A lag of 26 days is also found between $\rho(SSSA)$ and $\rho(SSTA)$ (Figure 5c), considering the appearance date as the date where the amplitude reaches half of its maximum intensity. Until the 11th of June, $\rho(SSSA)$ dominates over $\rho(SSTA)$. During the second part of the year (after August), the signal in SSS is much weaker while the one in SST lingers until the beginning of boreal autumn.

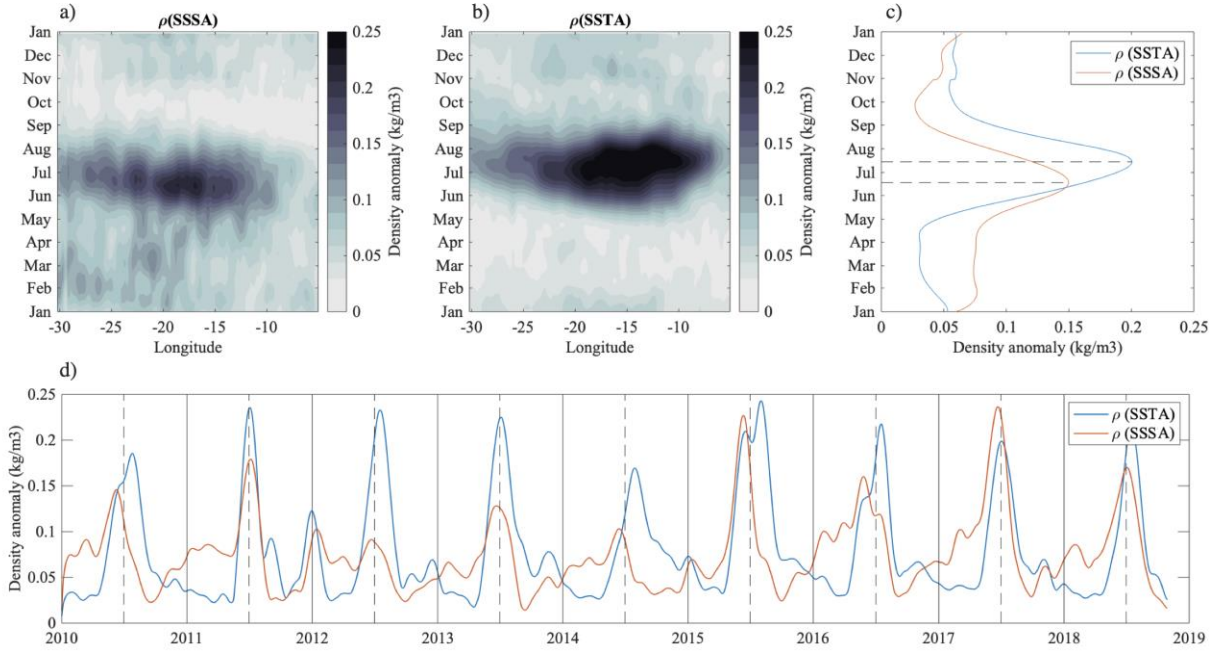

Figure 5: *Hovmöller diagrams of the 2010-2018 climatological SSSA (a) and SSTA (b) amplitudes contributions to surface density at 1°N. (c) corresponding 30°W-5°W longitude averaged climatologies for the contribution of SSS (orange) and SST (blue). (d) 9-year time series of the contribution of SSSA (orange) and SSTA (blue) to density averaged over 30°W-5°W longitude.*

3.3 Interannual variations of TIW properties and signature in SSS and SST

The relatively short 9-year long SSS and SST time-series provide some preliminary information on the interannual variability of TIWs (Figures 5d, 6). The Atlantic Ocean presents a large and complex interannual variability. While the SST variability associated with TIWs has been studied before (e.g. Perez et al., 2012), we have the opportunity to study the SSS variability and therefore the relative contribution of salinity to the density gradient and TIWs density anomaly.

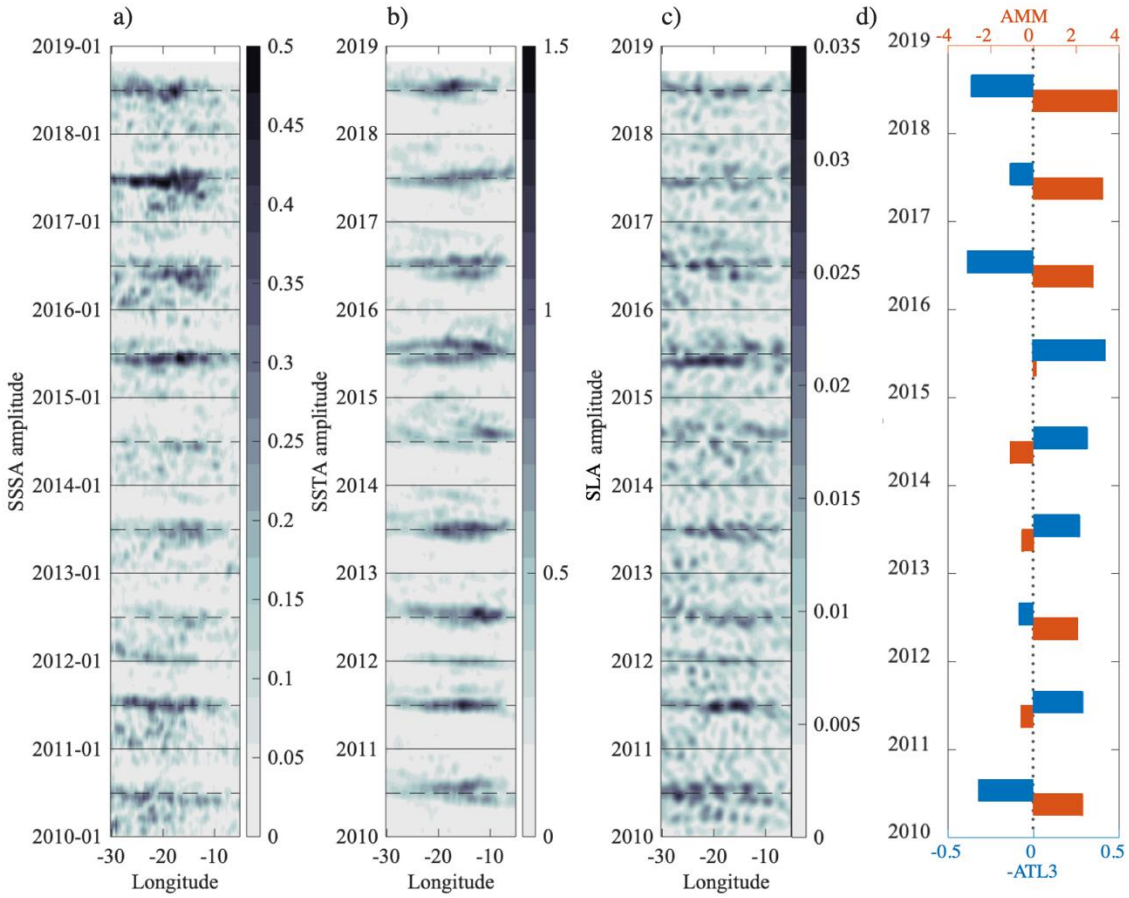

Figure 6: *2010-2018 Hovmöller diagrams at 1°N of a) SSSA amplitude, b) SSTA amplitude, c) SLA amplitude. The mean AMM index for the month of April-May-June (orange) and the opposite of the mean ATL3 index for the month of June-July-August (blue) are represented in d).*

Regarding the interannual variability of the amplitudes of SSSA, SSTA and SLA, three time-periods stand out (Figure 6). From 2012 to 2014, TIWs signature in salinity is low. On the opposite, the amplitude of SSSA is the strongest during the 2015-2018 time-period. 2010-2011 is characterized by moderate salinity amplitudes. The variations of the amplitude of SSTA and SLA do not present the same patterns as the one of SSSA. Indeed, in contrast to the amplitude of SSSA, both the ones of SSTA and SLA are weaker than usual from 2016 to 2018. The three datasets are nevertheless concordant in 2011, 2014 and 2015. In 2011 and particularly in 2015

384 they present stronger amplitude than usual, and the opposite happens in 2014. Overall, the
385 interannual variations of SLA are more correlated with the one in SSTA than in SSSA (SLA is
386 correlated to SSTA with a correlation coefficient of 0.6 and only of 0.25 with SSSA).
387 Interannual variations of $\rho(SSSA)$ reflect the ones of SSSA particularly well (Figure 5d).
388 $\rho(SSSA)$ is lower during the 2012-2014 period, and particularly large in 2011, 2015 and 2017.
389 $\rho(SSTA)$ follows the same variations as the amplitude of SSTA, but its year-to-year variations
390 are less pronounced. Changes in seasonality happen only in 2011, when $\rho(SSSA)$ peaks later
391 than usual and leads to the disappearance of the one-month gap between $\rho(SSSA)$ and $\rho(SSTA)$.
392 Thus, the interannual variability of the TIW signals at 1°N does not follow a unique pattern, with
393 changes in seasonality and intensity that can be different in SSS from SST. The results at this
394 latitude hold for nearby-latitudes (c.f. supplementary Figures S6, S7 and S8 showing high
395 correlation coefficient between the time series at 1°N and the ones at 0.5°N and 1.5°N, as well as
396 slightly smaller standard deviations at these other latitudes). The small interannual latitudinal
397 shifts of the SSS and SST fronts are thus not responsible for the changes between the SST and
398 SSS signals described above.
399
400 By a radon transform in the 30°W-5°W longitude range we compute a mean westward velocity
401 (averaged on SLA, SSS and SST for their common period of maximum intensity (6^{th} of June -
402 20^{th} of July, Figure 4, Figure S9)), of 0.4 m/s. The radon transform has been previously used in
403 several studies to compute the phase speed of waves (Cipollini et al., 2001; Caltabiano et al.,
404 2005; Yin et al., 2014) and is detailed in Hill et al. (2000). It gives the variance of the longitude-
405 time plot along a radial line oriented at a specific angle. Phase speed can then be obtained by
406 retrieving the angle of maximum variance. The phase speed of TIWs varies interannually. Such a

variability has been suggested by previous studies in the Pacific (Contreras, 2002; Lee et al., 2012; Yin et al., 2014). From 2010 to 2018, the respective wave speeds are : 0.35 (2010), 0.45 (2011), 0.3 (winter 2011-2012), 0.35 (2012), 0.35 (2013), 0.45 (2014), 0.4 (2015), 0.3 (2016), 0.45 (2017), 0.4 (2018), in m/s, reported to the closest 0.05 m/s. These estimations have to be used carefully as the speed of TIWs is also subject to considerable spatial variability, and the time-period over which it is estimated is not very long. It indeed changes with longitude, as phase speeds are usually faster in the east than in the west (Jochum et al., 2004), and with time, as they are faster in June than in September. What stands out is that waves propagate more rapidly in 2011, 2014 and 2017 and are slower in 2016.

3.4 Energetics of TIWs: PPE

TIW energy is associated with the total perturbation energy, sum of the perturbation kinetic energy and perturbation potential energy (PPE). Baroclinic instability converts energy between the background APE and the PPE. This is modulated by the density gradient. Previous satellite-based papers addressing the question of the energy delivered to the TIWs by the horizontal density gradient were limited by the lack of subsurface data. One approximate way to get around this problem is to use a definition of the PPE similar to the one for vertically-propagating internal waves, as done by Lee et al. (2014). However, with a focus on the energy extracted by TIWs from the horizontal density gradient, one should in particular consider what happens in the near-surface ocean, to which the approximate formula may not be relevant. This study is based on 9 years of data and includes sufficient Argo profiles in each climatological month to assume that our results are representative of the mean monthly situation during these 9 years. The Argo data provide vertical profiles of density anomalies associated with surface TIWs. Without doing any

assumption on the vertical density gradient, we compute the PPE at each point of the water column. However, below 60 m the signal becomes too uncertain to be analysed.

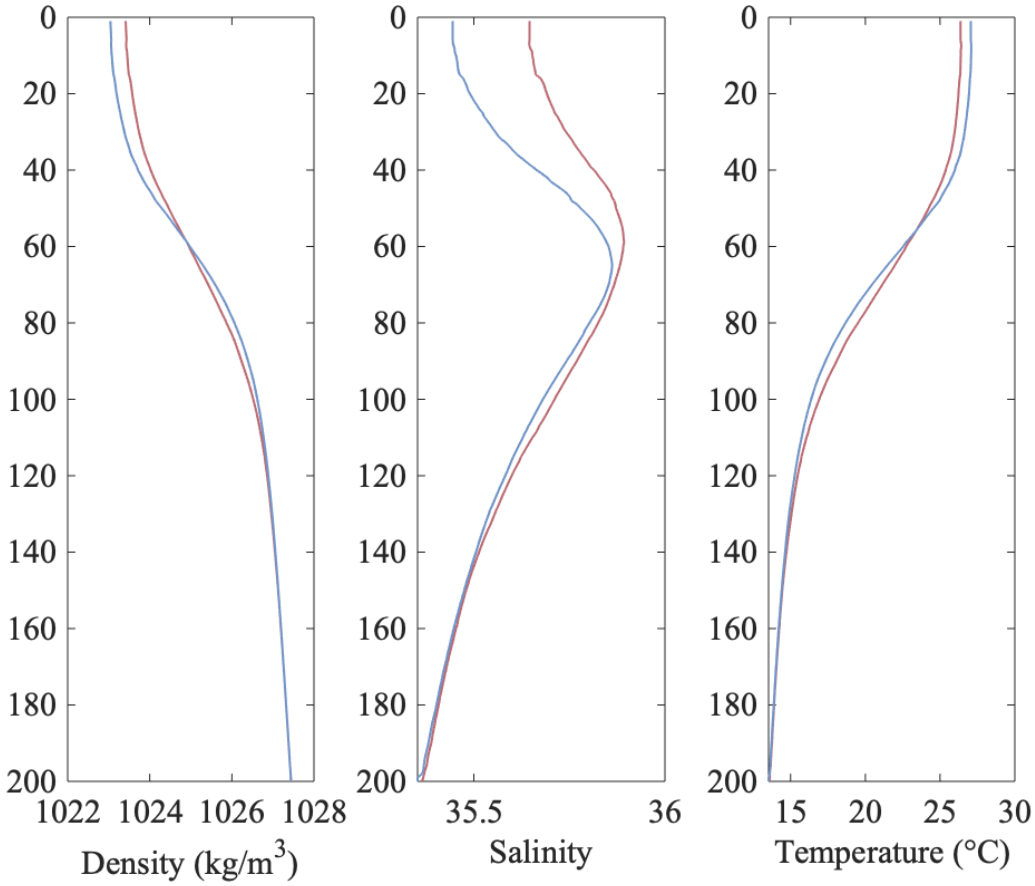

Figure 7: *Mean density (a), salinity (b) and temperature (c) Argo profiles located in a satellite detected positive (red) and negative (blue) tropical instability wave anomaly for May-June-July-August-September from 2010 to 2018.*

Based on the sign of the density anomaly associated with TIWs, profiles were sorted into two categories to create composites. Figure 7 presents the mean composites of the density, salinity and temperature profiles averaged in May-June-July-August-September located in a positive and negative TIW-related density anomaly. Near the surface, profiles in a positive density anomaly are saltier, colder and therefore denser than profiles in a negative density anomaly and correspond to characteristic profiles of upwelling conditions. Below 60 m, the sign of the

441 difference in temperature and density changes, but the uncertainty related to the scatter in the
442 dataset is too large, and the results are not significative.

443 Using the density anomaly profiles, we compute the total PPE (Equation 3) and the relative
444 contribution of salinity (Equation 4) and temperature (Equation 5) to PPE. Figure 8 shows the
445 integrated PPE on the surface-35 m layer (layer with surface salinity anomalies) and for the 35-
446 60 m layer. In both layers, the contribution to the integrated PPE is nearly equally distributed
447 between temperature and salinity. Therefore, not taking into account salinity underestimates the
448 total PPE by almost a factor of two. These results in the surface layer are similar to the ones
449 deduced by satellite observations from the amplitudes of $\rho(SSSA)$ and $\rho(SSTA)$ (Figure 5).

450 In the top layer, salinity and temperature contributions to PPE have the same overall magnitude
451 in May and June (Figure 8a). While the contribution of salinity stays almost constant in July, the
452 one of temperature reaches a strong maximum. Temperature contributes to two thirds of the total
453 PPE in July and August. Both contributions then decrease until September. A similar seasonal
454 variability is present at depth (Figure 8b). Salinity and temperature contributions are comparable
455 until July, and temperature then contributes slightly more than salinity to the total PPE.
456 Therefore, during the development phase of the TIWs, the salinity contribution to PPE is as
457 important as the temperature one. From July to September, the PPE is dominated by temperature
458 but the salinity signal is not negligible, with salinity contributing 30 to 45% of the total PPE.

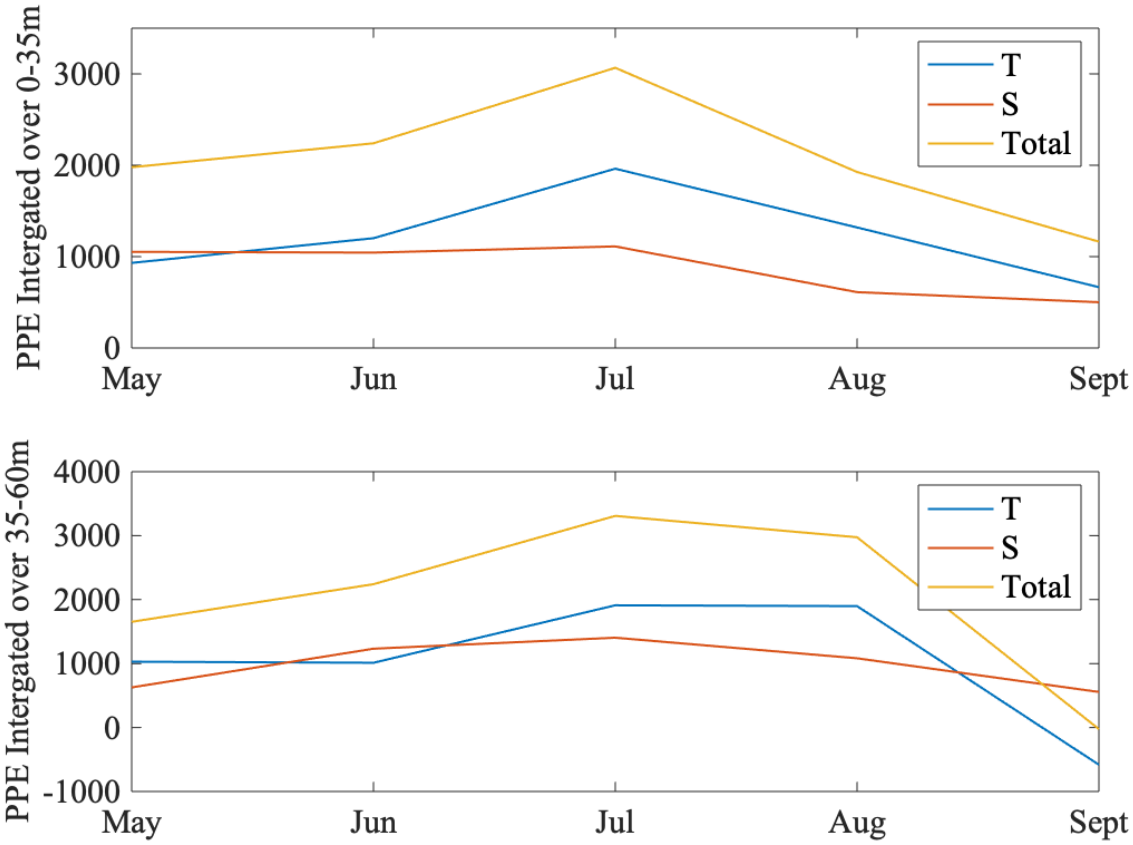

Figure 8: *Integrated perturbation potential energy on the top 35m of the water column (a) and on the 35-60m (b). PPE is represented in yellow; orange and blue describe respectively the contribution of salinity and temperature.*

The background APE, representing the energy available for baroclinic conversion, (supplementary Figure S10) is also subject to seasonal variations. The maximum APE is reached in June (one month earlier than PPE) for both layers, and decreases progressively until September. Temperature contribution the APE is slightly higher than the one of salinity, and is higher in the 35-60 m layer. The APE below 60 m is deeply influenced by the presence of the EUC which goes beyond the scope of this analysis.

4 Discussion

4.1 Mean seasonal cycle

The maximum of $\rho(SSTA)$ lags the one of $\rho(SSSA)$ by approximately one month (Figures 4 and 5). The maximum amplitude of SSSA is also observed one month before the SSTA one. At large scale, this lag between the maximum of SSS and the minimum of SST in the region of the Atlantic cold tongue has been observed by Schlundt et al., (2014), and studied by Da-Allada et al., (2017). From model data, they analysed the different terms of the salinity budget and found that the vertical mixing between the SEC and the EUC is mainly responsible for the salinification of the area in spring and summer. From further analysis of the EUC they showed that its erosion leads to the disappearance of its associated salinity maximum from July to September, reducing the contribution of vertical mixing and advective salinity flux into the mixed layer. Therefore, the surface signal in salinity starts to decrease in June–July, while the cold temperature signal is maintained up to July by the upwelling. This erosion of the equatorial salinity maximum during boreal summer was also reported by several authors based on observations and models (Gouriou & Reverdin, 1992; Kolodziejczyk et al., 2009; Johns et al., 2014). We suggest here that the large-scale seasonality of temperature and salinity influences the seasonality of mesoscale phenomena such as TIWs. It would induce a time difference of approximately one month between the maximum signals in salinity and in temperature at the surface, which is also the mean lag observed between $\rho(SSTA)$ and $\rho(SSSA)$ (Figure 5).This phenomenon can also explain the PPE seasonal cycle, with similar contribution of salinity and temperature in May-June followed by dominance of temperature in July-August.

As observed in part 3.4., the mean seasonal cycle of PPE as derived from Argo profiles (Figure 8) has the same shape as the one of $\rho(SSTA)$ and $\rho(SSSA)$ deduced from satellite observations (Figure 5c) but with a weaker amplitude. While salinity dominates the satellite surface density signal in May-June, it is indeed less the case using Argo profiles, with temperature and salinity contributing with a similar magnitude. The satellite data products represent SSS integrated over an area of 50x50 km^2 centred at 1°N, whereas we select Argo floats located in the 0°N-3°N latitudinal band. This sampling difference could lead to the observed difference in the respective salinity and temperature contributions. In salinity, TIWs are the most visible at 1°N (see supplementary Figure S6), therefore, even by trying to remove the effect of the meridional gradient on Argo profiles it is still possible that by combining data from this larger latitudinal band the Argo salinity signal is dampened. The temperature signal is also the most visible at 1°N, but is more persistent at higher latitudes than the SSS one (supplementary Figure S7) and could be less affected. Henceforth, it is possible that the influence of salinity is a little underestimated with respect to the one of temperature in the analysis using Argo data.

Satellite salinity and temperature are representative of the top surface layer of the ocean (less than 1-cm depth), whereas the Argo profiles uppermost values are at 5-m depth. Even though the near-surface vertical structure of TIWs is not well characterized, it is likely that there might be a slight horizontal shift between the surface and sub-surface structures. This might happen for the signal in temperature as a consequence of surface erosion and of the SST feedback on the air-sea fluxes, and for the signal in SSS as a consequence of rain induced surface stratification under the ITCZ.

4.2 Interannual variability

Discussing the interannual variability in the Equatorial Atlantic is challenging. Large scale SST, wind stress divergence and curl, and current shear indices hardly explain the interannual variability of near equatorial TIWs in SST and SLA (Perez et al., 2012). The tropical Atlantic Ocean variability is dominated by two major modes, the Atlantic Meridional Mode (AMM) and the Atlantic zonal mode, commonly referred as the Atlantic Niño mode. We first discuss the interannual variability in the amplitude of the waves, and then of their phase velocity, in light of these modes. We particularly focus on the variability in the TIW-related salinity anomalies, as it has not been studied before.

SSS in the tropical Atlantic is controlled by several seasonally varying processes among which high precipitation under the ITCZ and river discharge (Awo et al., 2018; Grodsky et al., 2020). Both processes are strongly influenced by precipitations, and the leading mode of interannual rainfall variability in the tropical Atlantic is the AMM (e.g. Grodsky & Carton, 2018). It peaks in spring and is related to a cross-equatorial gradient in SST (Ruiz-Barradas et al., 2000; Chiang & Vimont, 2004) that governs anomalous meridional atmospheric pressure differences and related shifts of the ITCZ which in turn affects rainfall. The mean spring (April-May-June) AMM index from NOAA is represented by orange bars in Figure 6d. A positive AMM index indicates an anomalous northward shift of the ITCZ. In consequence, precipitations are reduced close to the equator and rainfall enhanced north of the equator. We thus expect more contrasted SSS signals during positive AMM phases. However, the year to year AMM index does not present a strong correlation with the ASSSA. To understand why the relation holds better some years, it is also interesting to look at the AMM trend. Indeed, a decaying phase of the AMM leads to a

536 salinification north of the equator decreasing the salinity gradient at 1°N, whereas this gradient is
537 enhanced during the build-up phase (Grodsky & Carton, 2018). It will therefore enhance the
538 signal resulting from a positive or negative AMM index. During the period of interest here,
539 2010-2018, AMM goes mainly through two phases: a decaying phase (from positive to negative)
540 from 2012 to 2014 and a build-up phase (negative to positive) after 2014 (Figure 6d). These two
541 phases also correspond to the periods of low (before 2012-2014) and high (2015-2018)
542 amplitude of SSSA. Therefore, the decaying phase of the AMM accentuates the decrease of the
543 salinity gradient that we would expect for a negative AMM index, coherent with the low
544 amplitude of SSSA in 2013 and 2014. The opposite mechanism will enhance the salinity
545 gradient, and therefore the amplitude of SSSA as observed in 2016, 2017 and 2018.
546
547 The Atlantic Niño is the other main mode of variability in the tropical Atlantic. Several studies
548 have shown the dependency of the Pacific TIW intensity to the El Niño phenomenon
549 (Hashizume et al., 2001; Contreras, 2002; Wang & Fiedler, 2006; An, 2008). During El Niño
550 years, the decrease in SSS and SST gradients associated with weaker-than-usual easterly winds
551 and equatorial upwelling, is believed to generate less energetic TIWs. On the contrary, during la
552 Niña year, TIWs are intensified due to a stronger current shear at the equator and gradients are
553 more pronounced. The SSS and SST TIWs-related anomalies are thus enhanced (Contreras,
554 2002; Yin et al., 2014). Analogous mechanisms seem to occur in the Atlantic with the Atlantic
555 Niño dynamics, but with a less clear connexion (Perez et al., 2012). The opposite of the ATL3
556 index (Atlantic counterpart of the Pacific Niño3 index), as defined by Zebiak (1993) and
557 averaged over June-July-August is plotted in Figure 6d. The correlation with the amplitude of
558 SSSA, SSTA and SLA is unclear, with some years being in good agreement (2015) and others

559 years not so much (2014). The ATL3 index is in better agreement with SSTA and SLA than
560 SSSA. Even if the intensity of the ATL3 index is not well correlated to the amplitude of the
561 variable studied, 6 years out of 9 we observe an agreement between the sign of ATL3 and the
562 variations of SSTA and SLA. In 2011, 2013 and 2015, Atlantic Niña conditions correspond to
563 stronger amplitudes in SSTA and SLA and the opposite is observed in 2016, 2017 and 2018.
564
565 The variations of SSTA are more correlated with SLA than the one of SSSA. This suggests that
566 they are more influenced by dynamical processes (mainly linked to the cold tongue), while SSSA
567 is also impacted by precipitations, river discharge or different dynamics.
568
569 From 2010 to 2019, the two indexes tend to work in opposite way. The competition between the
570 two indexes can therefore partly explain the mixed results. A 9-year time series is too short to
571 unravel the parts played by the AMM and Atlantic Niño mode on the interannual variability of
572 SSSA, SSTA and SLA in such a complex environment. We can expect that with longer time
573 series and therefore more meaningful statistics we might be able to shed light on the phenomena
574 driving the interannual variability of TIWs in the tropical Atlantic.
575
576 Nevertheless, this study focusing mainly on the variability of the TIW-related salinity anomalies,
577 we will delve deeper into the understanding of two contrasted years that stands out of our time
578 series: 2015 and 2017. 2015 presents strong SSSA, SSTA and SLA (Figure 3), whereas 2017 is
579 characterized by strong SSSA but weak SSTA and SLA.
580

581 The very intense signature of TIWs on SSTA, SSSA and SLA in 2015 makes this year
582 particularly interesting (Figure 3). The good agreement between the three datasets emphasizes
583 the role of dynamical processes. According to the ATL3 index, 2015 is the strongest Atlantic
584 Niña year of the time-series. The observations present multiple characteristics coherent with an
585 Atlantic Niña phenomenon: enhanced SSTA, SSSA and in particular SLA; anomalies extended
586 further east than usual, SSTA and SLA persisting until late summer. Even if the correlation
587 between the TIWs interannual variability and ATL3 index is weak on the 9-year time series,
588 2015 is a year where Atlantic Niña conditions influence the TIWs for all variables.
589
590 In opposition to 2015, the amplitudes of SSTA and SLA are weaker than usual in 2017 whereas
591 strong SSSA amplitude is observed. The horizontal salinity gradient at the surface is strongly
592 enhanced, but not the temperature one. This year, the contribution of SSS to surface density
593 dominates over the SST one during the whole TIW season at 1°N (Figure 5d). When considering
594 the SSS anomaly maps for 2017 (supplementary Figure S11a) we observe unusual high SSS in
595 the equatorial band, between 0°W and 20°W which directly contributes to increasing the SSS
596 horizontal gradient. By considering precipitations over the ocean for the months of March-April-
597 May-June 2017 (supplementary Figure S11b), the correlation between the patterns of high
598 salinity - low precipitations and between low salinity - high precipitations is striking. The
599 equatorial salinification is associated with anomalously low precipitations. The high salinity
600 patch is slightly more latitudinally spread out than the precipitation one, probably due to
601 horizontal advection through Ekman transport. Between 16°W and 30°W, north of 3°N, negative
602 salinity anomalies associated with high precipitations anomalies (reaching $2mm.d^{-1}$) are indeed
603 observed sustaining this stronger than usual meridional SSS gradient. Precipitations as well as

dynamical processes may play a role in 2017. From July to September, lower TIW activity in SSTA and SLA at 1°N than averaged over the 2010-2019 period is observed. It is also the period were the upwelling is fully set up, although the cold tongue is weak in 2017 (positive ATL3 index) which reduces the SST contrast, therefore limiting the observation of TIWs in SST. The absence of TIWs observed at 4°N-23°W (Perez et al., 2019) from July to September support the results presented here at 1°N. The observation in salinity therefore deviates from the one in temperature due to the different processes that impact the meridional salinity and density gradient. While in 2017 the salinity gradient seems to be dominated by the precipitations north of the equator, the one in temperature is influenced by the cold tongue dynamics.

The phase speed of TIWs is also subject to interannual variations (Figure S9). On average TIWs propagate at 0.4 m/s which is an intermediate value between the Chelton et al. (2000) speed of 0.3 m/s estimated from microwave SST signals and Lee et al. (2014) speed of 0.5 m/s estimated from SSS, SST and SLA data for 2012-2013, and within the range reported by Jochum et al. (2004) (0.3-0.5 m/s). From 2010 to 2018 the TIW phase speeds vary within these bounds. A certain spread in the phase speed is expected as the waves are generated by an unstable flow field and not by a forcing with a distinct period. Therefore, the TIW properties such as the phase speed range, could result from variations in the properties of the most unstable barotropic or baroclinic modes (Jochum et al., 2004) which depend on the background state (stratification, shear). A change in this background state, seasonal or interannual, would modify the most unstable mode and thus the preferred phase speed. In particular, stronger upwelling and resulting deeper propagation layer (decrease of the stratification due to stronger vertical mixing) and stronger shear should modify the phase speed. Another hypothesis involves the variability of the

627 mean current at 1°N. The absolute pulsation depends on the mean flow. A stronger westward
628 flow at 1°N would hence accelerate the propagation speed of the TIWs. Links with the ATL3
629 index are however unclear. Enhanced upwelling and surface currents during Atlantic Niña years
630 lead most of the time to high phase speeds (2011, 2014, 2015 but not 2013), whereas the
631 opposite does not hold for Atlantic Niño years.
632
633 Satellite data provide a good analysis of the surface TIWs interannual variability, but cannot
634 describe the processes happening at subsurface. Unfortunately, the number of Argo profiles
635 limits the study of the subsurface variability. In order to have a significant number of profiles, we
636 aggregate the data acquired during two distinct periods, each period being characterized by a
637 strong surface salinity anomaly, with TIWs being much less visible in SSS in 2012-2014 than in
638 2015-2018. It allows us to obtain a significant number of profiles for each period, which makes
639 us confident in the results. By separating the profiles between these two periods, we observe that
640 the PPE in the top 35-m layer is dominated by temperature in 2012-2014 (PPE_T = 545 J. m^{-2} and
641 PPE_S = 231 J. m^{-2}) and salinity in 2015-2018 (PPE_T = 613 J. m^{-2} and PPE_S = 736 J. m^{-2}). PPE is
642 also larger in the top 35-m for the second period (1318 J. m^{-2} in 2015-2018 and 781 J. m^{-2} in
643 2012-2014). The high uncertainties linked with the low number of Argo profiles (especially in
644 2012-2014 where only 146 profiles are used) prevent us from dwelling further into the analysis.
645 Nevertheless, the interannual variability observed at the surface is consistent with the one
646 observed at subsurface, which is promising for further studies on the interannual variability with
647 longer time series and a greater number of profiles.

5 Conclusions

The SMOS satellite mission provides unprecedented observations of SSS over more than 10 years. By complementing this information with Aquarius and SMAP SSS, the CCI project derives a first combined multi-mission product from 2010 to the end of 2018. The ~50-km resolution of CCI SSS provides a good observation of large scale and mesoscale variability in the tropical Atlantic Ocean. CCI SSS data are able to well capture TIWs and their properties (propagation speed, length scale), in addition to SST and SLA data. In line with previous studies, 1°N is found to be the latitude at which waves are the most energetic. At this latitude, the mean 2010-2018 westward propagation speed is 0.4 m/s. SSS together with satellite-based SST are used to investigate the relative contributions of the two parameters to the meridional gradient of surface density generated by TIWs. Argo profiles are used to investigate the associated subsurface signals. In the top 60 m of the water column, salinity and temperature contributes in almost equal proportions to the PPE. Our study shows that even on a very well documented phenomenon such as the TIWs, the earlier lack of salinity observations of the waves was an issue impeding its full understanding. Not retaining salinity in the computation of PPE would underestimate the PPE by almost a factor 2. This implies that when trying to estimate the respective barotropic and baroclinic energy sources for the TIWs, not taking into account salinity would result in underestimating the baroclinic contribution.

The seasonal variability of TIWs in salinity and temperature differs, as the SSS anomalies generated by the waves peak approximately a month before the SST ones. This lag is also found in the relative contributions of SSS and SST to the density anomaly associated with the TIWs and to the TIW PPE. In May-June the contribution of SSS to PPE has the same magnitude as the

temperature one, at surface and at depth and therefore represents ~50% of total PPE. In July-August-September the relative contribution of salinity compared to the one of temperature decreases but still stays relevant and represents 30% to 45 % of the total PPE. An interesting next step in the study of TIW energetics would be to directly consider velocity to draw a more complete vision of the waves dynamics and total energy by including kinetic energy and estimating the baroclinic and barotropic conversion terms.

There is a large interannual variability modulating the seasonal signal, with different variations in SSS, SST and SLA. The Atlantic Meridional and zonal modes contribute to understand these variations for some specific years, such as in 2015, but hardly explain the totality of the interannual variability. Therefore, this 9-year long satellite SSS time series emphasizes the importance of having a long-term time series of satellite salinity. In order to remove the uncertainty concerning the role of the AMM and ATL3 in the interannual variability, a much longer time series (20 to 40 years) is needed. Moreover, the Argo coverage over 9 years is large enough to study the TIWs seasonality, but the analysis is still limited due to uncertainties. It is also too sparse to investigate in detail the interannual variability. Having access to the subsurface structure of TIWs significantly improves the understanding of the seasonal cycle. It also shows that the surface signal can be different from the subsurface one, underlining the complementarity between surface satellite and subsurface in situ data. It would therefore be very enriching to investigate the interannual signal in the same way, for example also including PIRATA mooring data. Furthermore, the SSS satellite product has a one-week temporal resolution. Improving this resolution could lower the smoothing of the wave in the product and better resolve the high frequency variability.

Acknowledgments

This work is a contribution to the Sea Surface Salinity Climate Change Initiative project (contract reference 4000123663/18/I-NB) supported by ESA and to the TOSCA/SMOS-Ocean project supported by CNES (Centre National d'Etudes Spatiales). We benefited from numerous data sets made freely available and listed here : the ESA CCI (European Space Agency Climate Change Initiative) version 1.8 (Sea_Surface_Salinity_cci, https://catalogue.ceda.ac.uk/uuid/9ef0ebf847564c2eabe62cac4899ec41), the OSTIA SST and the SLA produced by Ssalto/Duacs distributed by the CMEMS (https://resources.marine.copernicus.eu), the precipitation climatology project data provided by the NOAA/OAR/ESRL PSD (https://www.esrl.noaa.gov/psd/), the glob colour dataset distributed by ACRI-st (http://globcolour.info) and the Argo data collected and made freely available by the International Argo Program and the national programs that contribute to it (http://doi.org/10.17882/42182). Léa Olivier PhD grant is supported by the Ecole Normale Supérieure and Sorbonne Université. Audrey Hasson is supported by the ESA living planet fellowship. Useful discussions and comments from C. Thouvenin-Masson and A. Supply were appreciated. Helpful discussions with J.L. Vergely about the CCI product are acknowledged. We thank G. Foltz as well as the two reviewers for their interesting comments and suggestions.

References

Adler, R. F., Huffman, G. J., Chang, A., Ferraro, R., Xie, P.-P., Janowiak, J., et al. (2003). The version-2 global precipitation climatology project (GPCP) monthly precipitation analysis (1979–present). *Journal of Hydrometeorology*, *4*(6), 1147–1167.

An, S.-I. (2008). Interannual Variations of the Tropical Ocean Instability Wave and ENSO. *Journal of Climate*, *21*(15), 3680–3686. https://doi.org/10.1175/2008JCLI1701.1

Awo, F. M., Alory, G., Da-Allada, C. Y., Delcroix, T., Jouanno, J., Kestenare, E., & Baloïtcha, E. (2018). Sea surface salinity signature of the tropical Atlantic interannual climatic modes. *Journal of Geophysical Research: Oceans*, *123*(10), 7420–7437.

Behera, S., Brandt, P., & Reverdin, G. (2013). Chapter 15 - The Tropical Ocean Circulation and Dynamics. In G. Siedler, S. M. Griffies, J. Gould, & J. A. Church (Eds.), *International Geophysics* (Vol. 103, pp. 385–412). Academic Press. https://doi.org/10.1016/B978-0-12-391851-2.00015-5

Boutin, J., Vergely, J.-L., Marchand, S., d'Amico, F., Hasson, A., Kolodziejczyk, N., et al. (2018). New SMOS Sea Surface Salinity with reduced systematic errors and improved variability. *Remote Sensing of Environment*, *214*, 115–134.

Boutin, J., Vergely, J.-L., Koehler, J., Rouffi, F., & Reul, N. (2019). ESA Sea Surface Salinity Climate Change Initiative (Sea_Surface_Salinity_cci): Version 1.8 data collection. *Centre for Environmental Data Analysis*. https://doi.org/10.5285/9ef0ebf847564c2eabe62cac4899ec41

Caltabiano, A. C. V., Robinson, I. S., & Pezzi, L. P. (2005). Multi-year satellite observations of instability waves in the Tropical Atlantic Ocean. *Ocean Science Discussions*, *2*(1), 1–35.

Camara, I., Kolodziejczyk, N., Mignot, J., Lazar, A., & Gaye, A. T. (2015). On the seasonal variations of salinity of the tropical Atlantic mixed layer. *Journal of Geophysical Research: Oceans*, *120*(6), 4441–4462. https://doi.org/10.1002/2015JC010865

Chelton, D. B., Wentz, F. J., Gentemann, C. L., de Szoeke, R. A., & Schlax, M. G. (2000). Satellite microwave SST observations of transequatorial tropical instability waves. *Geophysical Research Letters*, *27*(9), 1239–1242.

Chelton, D. B., Esbensen, S. K., Schlax, M. G., Thum, N., Freilich, M. H., Wentz, F. J., et al. (2001). Observations of Coupling between Surface Wind Stress and Sea Surface Temperature in the Eastern Tropical Pacific. *Journal of Climate*, *14*(7), 1479–1498. https://doi.org/10.1175/1520-0442(2001)014<1479:OOCBSW>2.0.CO;2

Chelton, D. B., Schlax, M. G., & Samelson, R. M. (2011). Global observations of nonlinear mesoscale eddies. *Progress in Oceanography*, *91*(2), 167–216. https://doi.org/10.1016/j.pocean.2011.01.002

Chiang, J. C. H., & Vimont, D. J. (2004). Analogous meridional modes of atmosphere–ocean variability in the tropical Pacific and tropical Atlantic. *J. Climate*, *17*(21), 4143–4158.

Cipollini, P., Cromwell, D., Challenor, P. G., & Raffaglio, S. (2001). Rossby waves detected in

748 global ocean colour data. *Geophysical Research Letters*, *28*(2), 323–326.
749 Contreras, R. F. (2002, September 1). Long-Term Observations of Tropical Instability Waves
750 [research-article]. Retrieved June 3, 2020, from
751 https://journals.ametsoc.org/doi/abs/10.1175/1520-
752 0485%282002%29032%3C2715%3ALTOOTI%3E2.0.CO%3B2
753 Cox, M. D. (1980). Generation and propagation of 30-day waves in a numerical model of the
754 Pacific. *Journal of Physical Oceanography*, *10*(8), 1168–1186.
755 Da-Allada, C. Y., Alory, G., Penhoat, Y. du, Kestenare, E., Durand, F., & Hounkonnou, N. M.
756 (2013). Seasonal mixed-layer salinity balance in the tropical Atlantic Ocean: Mean state and
757 seasonal cycle. *Journal of Geophysical Research: Oceans*, *118*(1), 332–345.
758 https://doi.org/10.1029/2012JC008357
759 Da-Allada, C. Y., Jouanno, J., Gaillard, F., Kolodziejczyk, N., Maes, C., Reul, N., & Bourlès, B.
760 (2017). Importance of the Equatorial Undercurrent on the sea surface salinity in the eastern
761 equatorial Atlantic in boreal spring. *Journal of Geophysical Research: Oceans*, *122*(1), 521–538.
762 https://doi.org/10.1002/2016JC012342
763 de Decco, H. T., Torres Junior, A. R., Pezzi, L. P., & Landau, L. (2018). Revisiting tropical
764 instability wave variability in the Atlantic ocean using SODA reanalysis. *Ocean Dynamics*,
765 *68*(3), 327–345. https://doi.org/10.1007/s10236-017-1128-2
766 Donlon, C. J., Martin, M., Stark, J., Roberts-Jones, J., Fiedler, E., & Wimmer, W. (2012). The
767 operational sea surface temperature and sea ice analysis (OSTIA) system. *Remote Sensing of*
768 *Environment*, *116*, 140–158.
769 Düing, W., Hisard, P., Katz, E., Meincke, J., Miller, L., Moroshkin, K. V., et al. (1975).
770 Meanders and long waves in the equatorial Atlantic. *Nature*, *257*(5524), 280–284.
771 Durack, P. J., Wijffels, S. E., & Matear, R. J. (2012). Ocean Salinities Reveal Strong Global
772 Water Cycle Intensification During 1950 to 2000. *Science*, *336*(6080), 455–458.
773 https://doi.org/10.1126/science.1212222
774 Entekhabi, D., Njoku, E. G., O'Neill, P. E., Kellogg, K. H., Crow, W. T., Edelstein, W. N., et al.
775 (2010). The soil moisture active passive (SMAP) mission. *Proceedings of the IEEE*, *98*(5), 704–
776 716.
777 Foltz, G. R., Carton, J. A., & Chassignet, E. P. (2004). Tropical instability vortices in the
778 Atlantic Ocean. *Journal of Geophysical Research: Oceans*, *109*(C3).

779 https://doi.org/10.1029/2003JC001942
780 Font, J., Camps, A., Borges, A., Martín-Neira, M., Boutin, J., Reul, N., et al. (2009). SMOS: The
781 challenging sea surface salinity measurement from space. *Proceedings of the IEEE, 98*(5), 649–
782 665.
783 Gouriou, Y., & Reverdin, G. (1992). Isopycnal and diapycnal circulation of the upper equatorial
784 Atlantic Ocean in 1983–1984. *Journal of Geophysical Research: Oceans*, *97*(C3), 3543–3572.
785 https://doi.org/10.1029/91JC02935
786 Grodsky, S. A., & Carton, J. A. (2018). Delayed and quasi-synchronous response of tropical
787 Atlantic surface salinity to rainfall. *Journal of Geophysical Research: Oceans*, *123*(8), 5971–
788 5985.
789 Grodsky, S. A., Carton, J. A., Provost, C., Servain, J., Lorenzzetti, J. A., & McPhaden, M. J.
790 (2005). Tropical instability waves at 0 N, 23 W in the Atlantic: A case study using Pilot
791 Research Moored Array in the Tropical Atlantic (PIRATA) mooring data. *Journal of*
792 *Geophysical Research: Oceans*, *110*(C8).
793 Grodsky, S. A., Carton, J. A., & Bryan, F. O. (2014). A curious local surface salinity maximum
794 in the northwestern tropical Atlantic. *Journal of Geophysical Research: Oceans*, *119*(1), 484–
795 495. https://doi.org/10.1002/2013JC009450
796 Grodsky, S. A., Reul, N., Vandemark, D., & Bentamy, A. (2020). Intramonth oscillations of
797 Atlantic ITCZ observed in SMAP satellite salinity. *International Journal of Remote Sensing*,
798 *41*(3), 839–857.
799 Ham, Y.-G., & Kang, I.-S. (2011). Improvement of seasonal forecasts with inclusion of tropical
800 instability waves on initial conditions. *Climate Dynamics*, *36*(7), 1277–1290.
801 https://doi.org/10.1007/s00382-010-0743-0
802 Hashizume, H., Xie, S.-P., Liu, W. T., & Takeuchi, K. (2001). Local and remote atmospheric
803 response to tropical instability waves: A global view from space. *Journal of Geophysical*
804 *Research: Atmospheres*, *106*(D10), 10173–10185.
805 Hill, K. L., Robinson, I. S., & Cipollini, P. (2000). Propagation characteristics of extratropical
806 planetary waves observed in the ATSR global sea surface temperature record. *Journal of*
807 *Geophysical Research: Oceans*, *105*(C9), 21927–21945.
808 Im, S.-H., An, S.-I., Lengaigne, M., & Noh, Y. (2012). Seasonality of Tropical Instability Waves
809 and Its Feedback to the Seasonal Cycle in the Tropical Eastern Pacific [Research Article].

https://doi.org/10.1100/2012/612048

Jochum, M., & Murtugudde, R. (2006). Temperature Advection by Tropical Instability Waves. *Journal of Physical Oceanography*, *36*(4), 592–605. https://doi.org/10.1175/JPO2870.1

Jochum, M., Malanotte-Rizzoli, P., & Busalacchi, A. (2004). Tropical instability waves in the Atlantic Ocean. *Ocean Modelling*, *7*(1), 145–163. https://doi.org/10.1016/S1463-5003(03)00042-8

Jochum, M., Cronin, M. F., Kessler, W. S., & Shea, D. (2007). Observed horizontal temperature advection by tropical instability waves. *Geophysical Research Letters*, *34*(9). https://doi.org/10.1029/2007GL029416

Johns, W. E., Brandt, P., Bourlès, B., Tantet, A., Papapostolou, A., & Houk, A. (2014). Zonal structure and seasonal variability of the Atlantic Equatorial Undercurrent. *Climate Dynamics*, *43*(11), 3047–3069. https://doi.org/10.1007/s00382-014-2136-2

Johnson, G. C., Schmidtko, S., & Lyman, J. M. (2012). Relative contributions of temperature and salinity to seasonal mixed layer density changes and horizontal density gradients. *Journal of Geophysical Research: Oceans*, *117*(C4). https://doi.org/10.1029/2011JC007651

Kang, D., & Fringer, O. (2010). On the calculation of available potential energy in internal wave fields. *Journal of Physical Oceanography*, *40*(11), 2539–2545.

Katz, E. J. (1997). Waves along the equator in the Atlantic. *Journal of Physical Oceanography*, *27*(12), 2536–2544.

Kelly, B. G., Meyers, S. D., & O'Brien, J. J. (1995). On a generating mechanism for Yanai waves and the 25-day oscillation. *Journal of Geophysical Research: Oceans*, *100*(C6), 10589–10612. https://doi.org/10.1029/94JC02911

Kerr, Y. H., Waldteufel, P., Wigneron, J.-P., Delwart, S., Cabot, F., Boutin, J., et al. (2010). The SMOS mission: New tool for monitoring key elements ofthe global water cycle. *Proceedings of the IEEE*, *98*(5), 666–687.

Kolodziejczyk, N., Bourlès, B., Marin, F., Grelet, J., & Chuchla, R. (2009). Seasonal variability of the Equatorial Undercurrent at 10°W as inferred from recent in situ observations. *Journal of Geophysical Research: Oceans*, *114*(C6). https://doi.org/10.1029/2008JC004976

Kolodziejczyk, Nicolas, Hernandez, O., Boutin, J., & Reverdin, G. (2015). SMOS salinity in the subtropical North Atlantic salinity maximum: 2. Two-dimensional horizontal thermohaline variability. *Journal of Geophysical Research: Oceans*, *120*(2), 972–987.

841 https://doi.org/10.1002/2014JC010103
842 Lagerloef, G., Colomb, F. R., Le Vine, D., Wentz, F., Yueh, S., Ruf, C., et al. (2008). The
843 Aquarius/SAC-D mission: Designed to meet the salinity remote-sensing challenge.
844 *Oceanography*, *21*(1), 68–81.
845 Lee, T., Lagerloef, G., Gierach, M. M., Kao, H.-Y., Yueh, S., & Dohan, K. (2012). Aquarius
846 reveals salinity structure of tropical instability waves. *Geophysical Research Letters*, *39*(12).
847 Lee, T., Lagerloef, G., Kao, H.-Y., McPhaden, M. J., Willis, J., & Gierach, M. M. (2014). The
848 influence of salinity on tropical Atlantic instability waves. *Journal of Geophysical Research:*
849 *Oceans*, *119*(12), 8375–8394. https://doi.org/10.1002/2014JC010100
850 Legeckis, R. (1977). Long Waves in the Eastern Equatorial Pacific Ocean: A View from a
851 Geostationary Satellite. *Science*, *197*(4309), 1179–1181.
852 https://doi.org/10.1126/science.197.4309.1179
853 Legeckis, R., & Reverdin, G. (1987). Long waves in the equatorial Atlantic Ocean during 1983.
854 *Journal of Geophysical Research: Oceans*, *92*(C3), 2835–2842.
855 https://doi.org/10.1029/JC092iC03p02835
856 Lorenz, E. N. (1955). Available potential energy and the maintenance of the general circulation.
857 *Tellus*, *7*(2), 157–167.
858 Lumpkin, R., & Garzoli, S. L. (2005). Near-surface circulation in the Tropical Atlantic Ocean.
859 *Deep Sea Research Part I: Oceanographic Research Papers*, *52*(3), 495–518.
860 https://doi.org/10.1016/j.dsr.2004.09.001
861 Maritorena, S., d'Andon, O. H. F., Mangin, A., & Siegel, D. A. (2010). Merged satellite ocean
862 color data products using a bio-optical model: Characteristics, benefits and issues. *Remote*
863 *Sensing of Environment*, *114*(8), 1791–1804. https://doi.org/10.1016/j.rse.2010.04.002
864 Martin, M. J., Hines, A., & Bell, M. J. (2007). Data assimilation in the FOAM operational short-
865 range ocean forecasting system: a description of the scheme and its impact. *Quarterly Journal of*
866 *the Royal Meteorological Society: A Journal of the Atmospheric Sciences, Applied Meteorology*
867 *and Physical Oceanography*, *133*(625), 981–995.
868 Martinez, E., Raapoto, H., Maes, C., & Maamaatuaihutapu, K. (2018). Influence of Tropical
869 Instability Waves on Phytoplankton Biomass near the Marquesas Islands. *Remote Sensing*, *10*(4),
870 640. https://doi.org/10.3390/rs10040640
871 McCreary Jr, J. P., & Yu, Z. (1992). Equatorial dynamics in a 212-layer model. *Progress in*

Oceanography, *29*(1), 61–132.

Menkes, C. E., Kennan, S. C., Flament, P., Dandonneau, Y., Masson, S., Biessy, B., et al. (2002). A whirling ecosystem in the equatorial Atlantic. *Geophysical Research Letters*, *29*(11), 48-1-48–4. https://doi.org/10.1029/2001GL014576

Murray, J. W., Barber, R. T., Roman, M. R., Bacon, M. P., & Feely, R. A. (1994). Physical and Biological Controls on Carbon Cycling in the Equatorial Pacific. *Science*, *266*(5182), 58–65. https://doi.org/10.1126/science.266.5182.58

Murtugudde, R., & Busalacchi, A. J. (1998). Salinity effects in a tropical ocean model. *Journal of Geophysical Research: Oceans*, *103*(C2), 3283–3300. https://doi.org/10.1029/97JC02438

Musman, S. (1992). Geosat altimeter observations of long waves in the equatorial Atlantic. *Journal of Geophysical Research: Oceans*, *97*(C3), 3573–3579.

Perez, R. C., Lumpkin, R., Johns, W. E., Foltz, G. R., & Hormann, V. (2012). Interannual variations of Atlantic tropical instability waves. *Journal of Geophysical Research: Oceans*, *117*(C3). https://doi.org/10.1029/2011JC007584

Perez, R. C., Foltz, G. R., Lumpkin, R., & Schmid, C. (2019). Direct measurements of upper ocean horizontal velocity and vertical shear in the tropical North Atlantic at 4 N, 23 W. *Journal of Geophysical Research: Oceans*, *124*(6), 4133–4151.

Philander, S. G. H. (1976). Instabilities of zonal equatorial currents. *Journal of Geophysical Research (1896-1977)*, *81*(21), 3725–3735. https://doi.org/10.1029/JC081i021p03725

Philander, S. G. H. (1978). Instabilities of zonal equatorial currents, 2. *Journal of Geophysical Research: Oceans*, *83*(C7), 3679–3682. https://doi.org/10.1029/JC083iC07p03679

Piepmeier, J. R., Focardi, P., Horgan, K. A., Knuble, J., Ehsan, N., Lucey, J., et al. (2017). SMAP L-band microwave radiometer: Instrument design and first year on orbit. *IEEE Transactions on Geoscience and Remote Sensing*, *55*(4), 1954–1966.

Qiao, L., & Weisberg, R. H. (1995). Tropical instability wave kinematics: Observations from the Tropical Instability Wave Experiment. *Journal of Geophysical Research: Oceans*, *100*(C5), 8677–8693. https://doi.org/10.1029/95JC00305

Reul, N., Grodsky, S. A., Arias, M., Boutin, J., Catany, R., Chapron, B., et al. (2020). Sea surface salinity estimates from spaceborne L-band radiometers: An overview of the first decade of observation (2010–2019). *Remote Sensing of Environment*, *242*, 111769.

Reverdin, G., Kestenare, E., Frankignoul, C., & Delcroix, T. (2007). Surface salinity in the

Atlantic Ocean (30°S–50°N). *Progress in Oceanography*, *73*(3), 311–340. https://doi.org/10.1016/j.pocean.2006.11.004

Ruiz-Barradas, A., Carton, J. A., & Nigam, S. (2000). Structure of interannual-to-decadal climate variability in the tropical Atlantic sector. *Journal of Climate*, *13*(18), 3285–3297.

Schlundt, M., Brandt, P., Dengler, M., Hummels, R., Fischer, T., Bumke, K., et al. (2014). Mixed layer heat and salinity budgets during the onset of the 2011 Atlantic cold tongue. *Journal of Geophysical Research: Oceans*, *119*(11), 7882–7910. https://doi.org/10.1002/2014JC010021

Seo, H., & Xie, S.-P. (2011). Response and impact of equatorial ocean dynamics and tropical instability waves in the tropical Atlantic under global warming: A regional coupled downscaling study. *Journal of Geophysical Research: Oceans*, *116*(C3). https://doi.org/10.1029/2010JC006670

Seo, H., Jochum, M., Murtugudde, R., Miller, A. J., & Roads, J. O. (2007). Feedback of Tropical Instability-Wave-Induced Atmospheric Variability onto the Ocean. *Journal of Climate*, *20*(23), 5842–5855. https://doi.org/10.1175/JCLI4330.1

Steger, J. M., & Carton, J. A. (1991). Long waves and eddies in the tropical Atlantic Ocean: 1984–1990. *Journal of Geophysical Research: Oceans*, *96*(C8), 15161–15171. https://doi.org/10.1029/91JC01316

Strutton, P. G., Ryan, J. P., & Chavez, F. P. (2001). Enhanced chlorophyll associated with tropical instability waves in the equatorial Pacific. *Geophysical Research Letters*, *28*(10), 2005–2008. https://doi.org/10.1029/2000GL012166

Von Schuckmann, K., Brandt, P., & Eden, C. (2008). Generation of tropical instability waves in the Atlantic Ocean. *Journal of Geophysical Research: Oceans*, *113*(C8).

Wang, C., & Fiedler, P. C. (2006). ENSO variability and the eastern tropical Pacific: A review. *Progress in Oceanography*, *69*(2–4), 239–266.

Weisberg, R. H., & Weingartner, T. J. (1988). Instability Waves in the Equatorial Atlantic Ocean. *Journal of Physical Oceanography*, *18*(11), 1641–1657. https://doi.org/10.1175/1520-0485(1988)018<1641:IWITEA>2.0.CO;2

Wen, C., Xue, Y., & Kumar, A. (2012). Ocean–Atmosphere Characteristics of Tropical Instability Waves Simulated in the NCEP Climate Forecast System Reanalysis. *Journal of Climate*, *25*(18), 6409–6425. https://doi.org/10.1175/JCLI-D-11-00477.1

Yin, X., Boutin, J., Reverdin, G., Lee, T., Arnault, S., & Martin, N. (2014). SMOS Sea Surface

934 Salinity signals of tropical instability waves. *Journal of Geophysical Research: Oceans*, *119*(11),
935 7811–7826. https://doi.org/10.1002/2014JC009960
936 Yu, L. (2015). Sea-surface salinity fronts and associated salinity-minimum zones in the tropical
937 ocean. *Journal of Geophysical Research: Oceans*, *120*(6), 4205–4225.
938 https://doi.org/10.1002/2015JC010790
939 Zebiak, S. E. (1993). Air–sea interaction in the equatorial Atlantic region. *Journal of Climate*,
940 *6*(8), 1567–1586.

941